Initial State Interaction in the ($π^+$,3p) Reaction on N, Ar and Xe

B. Kotliński[8], D. Androić[9], G. Backenstoss[1], D. Bosnar[9], H. Breuer[4], H. Döbbeling[8], T. Dooling[7], M. Furić[9], P.A.M. Gram[3], N.K. Gregory[5], A. Hoffart[2,8], C.H.Q. Ingram[8], A. Klein[7], K. Koch[8], J. Köhler[1], M. Kroedel[1], G. Kyle[6], A. Lehmann[1,8], A.O. Mateos[5], K. Michaelian[8], T. Petković[9], M. Planinić[9], R.P. Redwine[5], D. Rowntree[5], U. Sennhauser[8], N. Šimičević[5], R. Trezeciak[2], H. Ullrich[2], H.J. Weyer[1,8], M. Wildi[1], K.E. Wilson[5],
(LADS collaboration)

[1] University of Basel, CH-4056 Basel, Switzerland
[2] University of Karlsruhe, D-76128 Karlsruhe, Germany
[3] LAMPF, Los Alamos NM 87545, USA
[4] University of Maryland, College Park MD 20742, USA
[5] Massachusetts Institute of Technology, Cambridge MA 02139, USA
[6] New Mexico State University, Las Cruces NM 88003, USA
[7] Old Dominion University, Norfolk VA 23529, USA
[8] Paul Scherrer Institute, CH-5232 Villigen PSI, Switzerland
[9] University of Zagreb, HR-10000 Zagreb, Croatia

Abstract. The pion absorption reaction ($π^+$,3p) on Ar was studied at pion energies of 70, 118, 162 and 239 MeV, and on N and Xe at 239 MeV. The $3p$ cross section with a 50 MeV cut on the missing energy is presented. The existence of an initial state interaction (ISI) component to the reaction was investigated. The portion of the $3p$ cross section assigned to the ISI process is less than one half and at lower energies significantly so.

PACS. 25.80.Ls Pion inclusive scattering and absorption

I Introduction

The primary process in pion absorption on heavy nuclei ($A > 10$) is thought to be the two nucleon absorption (2NA) quasi-deuteron mode. However, several past experiments have shown that the 2NA cross section does not exhaust the total absorption cross section [1–3]. Pion absorption with the emission of more than two energetic nucleons (multi-nucleon absorption) was observed in experiments [4–6] detecting at least three final state protons. From these data it is known that the strength of multi-nucleon absorption across the Δ-resonance region is significant and increases with nuclear mass and with incident pion energy. Though we have a broad knowledge of the strength of multi-nucleon absorption its detailed origin is still not clear [7,8].

One important question in this context is how much cascade processes contribute. Both initial state interactions (ISI), where the incident pion scatters on a nucleon before being absorbed by conventional 2NA, and final state interactions (FSI), where one of the outgoing nucleons from 2NA interacts with another nucleon in the nucleus, can lead to three energetic particles in the final state (3NA). Estimates of the expected FSI strength based on the nucleon-nucleus potential [9,10] suggested that this process alone could not account for the multi-nucleon strength, and this was confirmed experimentally [11]. Early searches for direct evidence of ISI or FSI were not conclusive. Tacik et al. [4], in an experiment detecting three protons from a carbon target, concluded that the bulk of the data could be described by a three nucleon phase space simulation. On the other hand, Brückner et al. [12] found evidence for the ISI process in pion absorption on carbon nuclei, but the strength appeared to be weak compared to the total absorption cross section. Burger et al. [2] limited the ISI process on Ni at 160 MeV to be less than 10% of the total cross section. However, past experiments suffered from limitations in phase space coverage, kinematic definition or statistical accuracy for the multi-nucleon channels. In recent publications [13,14] we have shown the existence of the ISI process in pion absorption on ^{3}He and ^{4}He nuclei. Evidence for the existence of ISI in pion absorption on N and Ar has been also reported [15] by our collaboration.

In the present paper we report results for the ($π^+$,3p) reaction on N, Ar and Xe at various pion energies. The N and Xe data are presented for a single incident pion energy of 239 MeV, and the Ar data for four pion energies
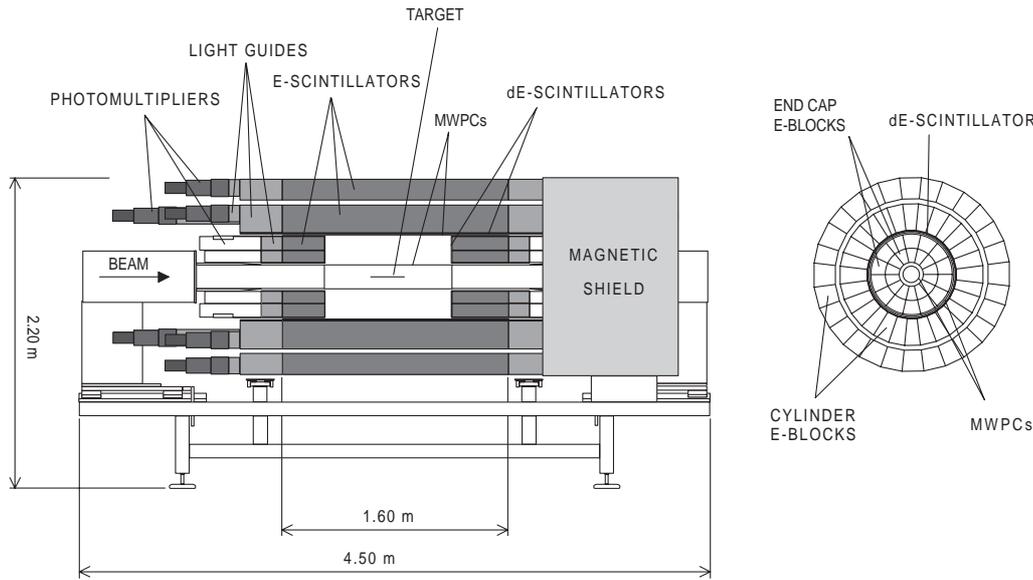
Fig. 1. A schematic view of the LADS detector

70, 118, 162 and 239 MeV. The data were analyzed for signatures of ISI and FSI processes.

II Experiment

The measurements were performed with the Large Acceptance Detector System (LADS) [16], which was built at the Paul Scherrer Institute (PSI) in Villigen, Switzerland to investigate multi-nucleon pion absorption (Fig. 1). With the solid angle coverage of more than 98% of 4π and the low proton threshold of about 20 MeV, a large fraction of the phase space was accessible to LADS even at low incident pion energies.

The detector consisted of a plastic scintillator cylinder divided into 28 $\Delta E - E - E$ sectors, each 1.6 m in active length. The ends of the cylinder were closed by end-caps, each consisting of 14 $\Delta E - E$ plastic scintillator sectors. The scintillators stopped normally incident protons of up to 250 MeV. The trajectory information for charged particles was provided by two coaxial cylindrical multiwire proportional chambers (MWPCs) inside the plastic cylinder. Their angular resolution was about 1° FWHM. The target was a high pressure (up to 100 bar) gas cylinder of 25.7 cm length and 2 cm radius with carbon-fibre/epoxy walls of only 0.5 mm thickness to keep background and particle thresholds low. A multi-coincidence trigger logic allowed specific final states of interest to be emphasized according to their charged and neutral multiplicities.

The π^+ beam was defined by a set of plastic scintillation detectors that counted the individual pions and removed particles in the beam halo. About 5% of the typical incident flux of about 3×10^6 momentum-analyzed pions per second was finally accepted by a 2 cm diameter scintillator placed about 50 cm upstream of the target centre.

For the three target nuclei studied, N, Ar, and Xe, the target gas pressure was 40 bar, 28 bar, and 13 bar, respectively. The target temperature and pressure were monitored during the experiment and stayed constant within less than 1% throughout each specific target/beam run.

III Data analysis

A Data treatment

The vertex of each event was reconstructed with the trajectory information measured by the MWPCs. Only events with track information for at least two charged particles, and thus with a well-defined vertex, were accepted. The spatial vertex resolution of less than 1 mm FWHM allowed a very efficient elimination of background events originating in the target walls (see Fig. 2). The narrow peaks at -11 cm and +14 cm in Fig. 2 correspond to events originating in the target walls, the plateau between represents events from the Ar target, and the background outside the peaks consists of events from air. Only events inside a volume of 100 mm upstream and downstream of the target centre and 15 mm around the beam axis were used in the data analysis. In order to estimate the remaining background from the target walls, data taken with an empty target were analyzed in the same way as was the full target data. For the $3p$ final state the empty target background was very small (*e.g.* 0.3% at 239 MeV). To eliminate events near the edge of the detector acceptance the polar angular range of the data was limited between 15° and 165°. With this cut the solid angle covered was reduced slightly to 96.6% of 4π.

The data from each individual scintillator channel were calibrated to have the same gain and timing. A direct calibration of the heavy target data was not possible due to the lack of a well-resolved excitation spectrum line, and so the calibration constants obtained from ^{2}H and He data were used [14]. A total energy resolution of about 3% FWHM was achieved.

For the separation of protons from other charged particles, such as pions and deuterons, conventional $E - dE/dx$
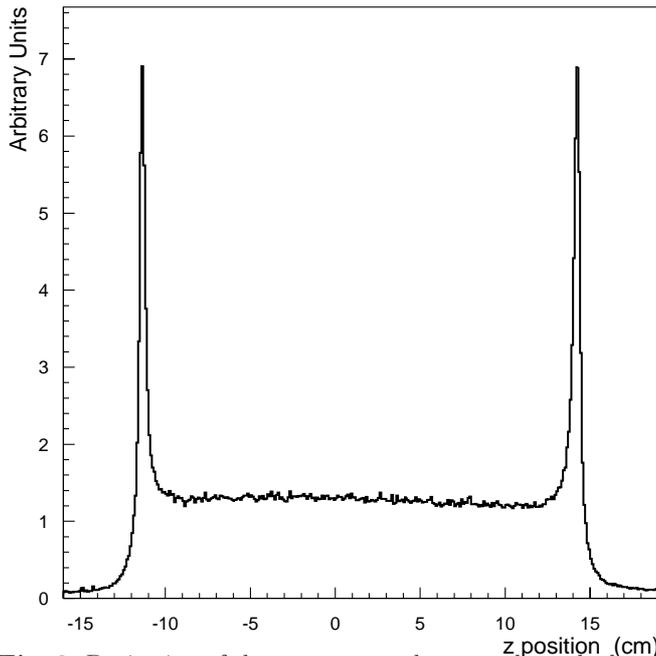
Fig. 2. Projection of the reconstructed vertex along the beam axis (z) for the Ar$(\pi^+,3p)$ reaction at $T_\pi = 239$ MeV. The two sharp peaks reflect events from the target entrance and exit walls

Fig. 4. The reduced time of flight (for a 30 cm flight path) of neutral particles plotted for the π^+ - Ar reaction at 118 MeV. The sharp peak at $1/\beta=1$ corresponds to photons and the broad peak around $1/\beta=4$ to neutrons

and $E-TOF$ (time of flight) particle identification (PID) techniques were applied. The latter method was used for all charged particles with less than 10 MeV light deposited in the E-scintillators, because these were stopped in or just passed through the thin ΔE-counters. Fig. 3 shows the separation of the charged pions from protons and
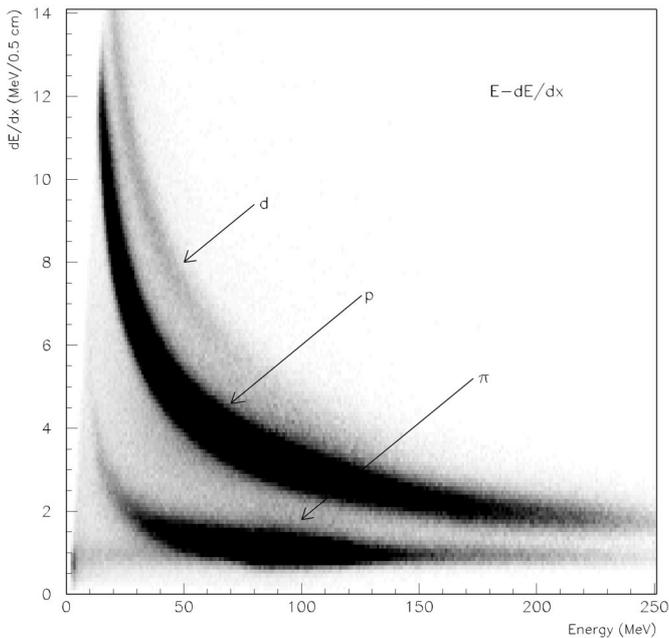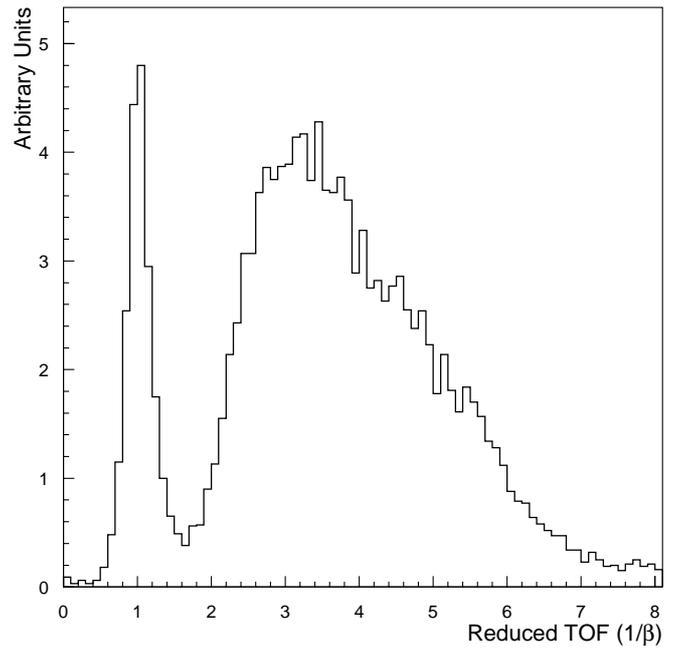

Fig. 3. The plastic scintillator $E - dE/dx$ PID plot for the interaction of 239 MeV π^+'s with N

deuterons obtained using the $E-dE/dx$ method. The plot is dominated by the protons and pions but the deuteron band can also be clearly identified. In the case of heavy targets the particle identification method is crucial in the analysis process since, contrary to the case of He, no powerful kinematic methods (*e.g.* missing mass cuts) are available to remove background.

The neutral particles were separated into neutrons and photons by a cut on the reduced time of flight shown in Fig. 4. Particles with a reduced time of flight below this cut (typically around 1.5) were identified as photons and those above as neutrons. Neutral signals with less than 5 MeV of deposited light were assumed to be noise and ignored. Photons which deposited more than 10 MeV of light in the scintillators were taken to originate from neutral pions, while those depositing less energy were assumed to be emitted by nuclear deexcitation. The neutron kinetic energy was calculated from its time of flight, and if less than 15 MeV then it was assumed to come from an evaporation processes.

Pion absorption events were selected from other reaction channels by vetoing events with charged or neutral (identified by high energy photons) pions. Due to the photon detection efficiency (about 30%) some of the neutral pions were not detected and therefore such events remained in the absorption event sample; this will be discussed below. In the next step of the data analysis events with three and only three energetic protons were selected. In these reactions, the recoil nucleus was in general produced in a highly excited state. Subsequently it decayed to its ground state with the emission of low energy par-
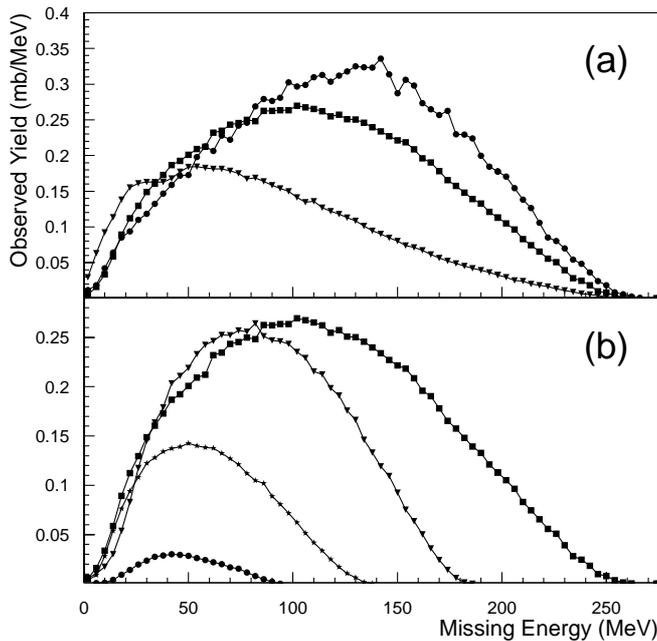
Fig. 5. The measured missing energy for the $(\pi^+,3p)$ reaction. In the upper part **a** the yields from the N target (*triangles*), the Ar target (*squares*) and the Xe target (*circles*) at $T_\pi = 239$ MeV are compared. In the lower part **b** the yields from the Ar target at 70 MeV (*circles*), 118 MeV (*stars*), 162 MeV (*triangles*) and 239 MeV (*squares*) are compared
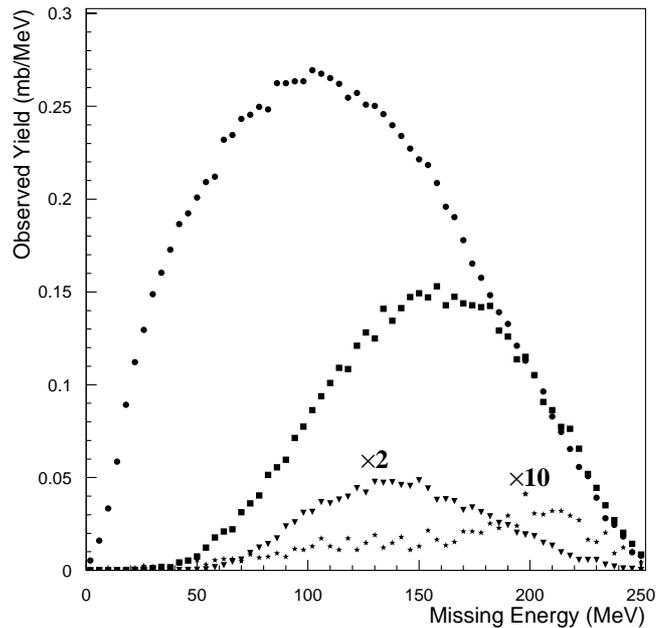
Fig. 6. The measured missing energy for the $Ar(\pi^+,3p)$ reaction (*circles*) at 239 MeV is compared with the $3pn$ channel (*squares*), $3p\pi^o$ channel (*stars*) and the $4p$ channel (*triangles*). The $3pn$ data have been adjusted for the neutron detection efficiency to indicate the expected amount of background. For better visibility the $3p\pi^o$ data are multiplied by 10 and the $4p$ data by 2

ticles like photons, protons, neutrons or even deuterons and alphas. In the selection and analysis of the absorption events here photons of less than 10 MeV, neutrons of less than 15 MeV, and protons and deuterons of less than 30 MeV, were ignored. The magnitude of the 30 MeV proton and deuteron threshold was selected to provide a uniform threshold over the whole detector. Our definition of a three proton ($3p$) event was thus: three energetic protons ($T_p > 30$ MeV), no deuterons above 30 MeV, no neutrons above 15 MeV, and no detected pions.

This $3p$ event sample includes contaminations from the following sources:

- $3p\pi^0$ events, where the π^0 was undetected;
- $3pn$ events, where the neutron was undetected;
- $4p$ events, where one proton was below threshold or outside the acceptance of the detector;
- $2p\pi^+$ events, where the π^+ was misidentified;
- $2pd$ events, where the d was misidentified;

In order to obtain a clean $3p$ data sample a missing energy cut was introduced. The missing energy is defined as:

$$E_{miss} = T_\pi + m_\pi - \sum_i T_p^i + Q$$

where T_π is the pion kinetic energy, m_π the pion mass, T_p^i the proton kinetic energy with the summation over the three detected protons and Q the reaction Q-value. In the case when all particles emitted in the reaction are detected, this quantity is almost equal to the excitation

energy of the residual nucleus (the difference is the kinetic energy of the recoiling nucleus, which is small). The measured missing energy distributions are shown in Fig. 5. In part a of this figure the yields from the three targets N, Ar and Xe at a π^+ beam energy of 239 MeV are shown; the distributions are seen to be quite different. For the light nucleus N the data are concentrated around low excitation energy with some structure around the excitation energy of 25 MeV being visible. For the Ar data the missing energy peak moves to 100 MeV and for Xe to 140 MeV with no trace of low energy structures. The increase in the average missing energy with the target mass is consistent with the data of Jones et al. [6]. In part b of Fig. 5 the measurements at the four beam energies 70, 118, 162 and 239 MeV for the Ar target are shown. The average value and the range of the missing energy, as expected, increase with the pion beam energy.

The data in Fig. 5 have been normalised to the incident beam and target thickness, and corrected for the average detector acceptance for the missing energy region 0-50 MeV. However, the acceptance will change significantly at higher missing energies, and this has not been taken into account in these spectra, because of the difficulty of doing so reliably. Thus the shape of the spectra will be increasingly biased by the changing acceptance at higher missing energies. Hence the vertical axis in Fig. 5 is labelled "observed yield" and not "cross section", as are those in Fig. 6 - 8 for similar reasons.
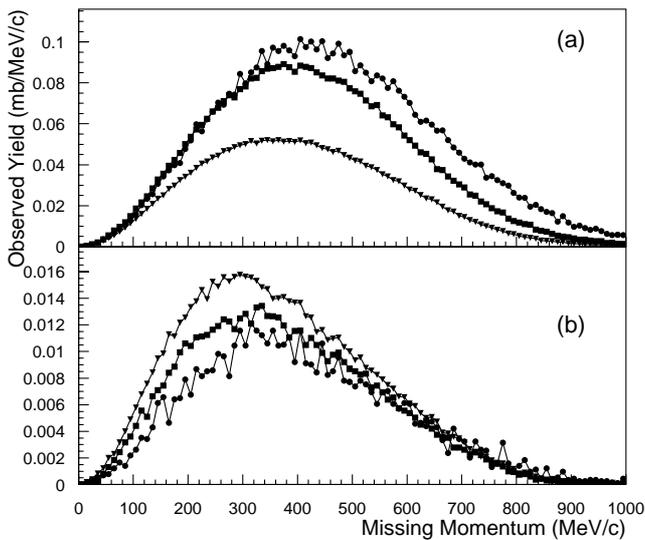
Fig. 7. The measured missing momentum plotted **a** for N (*triangles*), Ar (*squares*) and Xe (*circles*) at π^+ energy of 239 MeV. In the lower part **b** the same data are plotted but with the 50 MeV cut on the missing energy

The missing energy cut, used to select the $3p$ events, was chosen to be 50 MeV. Its value was a compromise between the demand for high data statistics and the purity of the $3p$ event sample. As a test the $4p$, $3pn$ and $3p\pi^0$ data were analyzed in a way similar to the $3p$ events; that is, only three protons were taken into account to calculate E_{miss}. The resulting missing energy plots are shown in Fig. 6. Only a small contamination from the three processes survives the 50 MeV cut. For $2p\pi^+$ events simulations were done where the π^+ was misidentified as a proton. The E_{miss} calculated from such events tends to

Fig. 8. The measured missing momentum plotted **a** for Ar at π^+ energy of 70 MeV (*squares*), 118 MeV (*stars*), 162 MeV (*triangles*) and 239 MeV (*circles*). In the lower part **b** the same data are plotted but with the 50 MeV cut on the missing energy

be located at much higher missing energy above the pion mass with only the reaction tails extending below. The 50 MeV cut is very efficient in suppressing this reaction channel as well, with the contamination level being below 0.1%. For the $2pd$ events the deuteron can be misidentified as a proton. In this case the missing energy cut is not effective since the $2pd$ data have an E_{miss} distribution similar to that of the $3p$ data. Simulations show that about 1% of the $2pd$ events appear as $3p$ events. With the observed $2pd$ yield being about 50% of the $3p$ yield, the amount of the misidentified $2pd$ events in the $3p$ event sample is about 0.5%.

Another variable describing the global characteristics of an event is the missing momentum. This is defined as :

$$\vec{P}_{miss} = \vec{p}_\pi - \sum_i \vec{p}_p^{\,i}$$

where $\vec{p}_\pi$ is the pion momentum and $\vec{p}_p^{\,i}$ are the momenta of the three detected protons. In the upper part a of Fig. 7 the magnitude of the missing momentum is plotted for the three targets at the same π^+ energy of 239 MeV. In the lower part b of the same figure the same data are plotted but with the cut limiting the missing energy to 50 MeV. The effect of the missing energy cut can be clearly seen, the peak moving to lower momenta with smaller tails in the region between 800-1000 MeV/c. No additional cuts were used to limit events with high missing momentum. The reason for this was two-fold: first, it was not clear where to choose such a cut; second, our simple Monte Carlo event generators, described in Sect. C, reproduced the measured missing momentum assuming simple parametrizations of the initial momentum distribution consistent with previous experiments. In Fig. 8 the missing momentum is shown for the Ar target at the four π^+ beam momenta. Again, part b of the figure shows the data after the 50 MeV E_{miss} cut was applied. As in the missing energy plots, the missing momentum data show some modest variation as a function of target mass, while the variation (especially of the large momentum tail) is large as a function of pion beam energy.

Additional information related to the data analysis presented here can be found in reference [18].

B Normalization

The measured yields were normalized to the number of incident pions and target nuclei in order to determine cross sections. The procedure was the same as the one described in our earlier publications [13,14]. The reliability of this procedure was verified by determining the well known pion absorption cross section on deuterium.

The number of target nuclei was determined from the target gas pressure and temperature. The areal densities varied from 4×10^{22} nuclei/cm^2 for N to 6×10^{21} nuclei/cm^2 for Xe. The estimated uncertainty on the number of scattering centers is 1% and comes mostly from the accuracy of the pressure and temperature measurements.
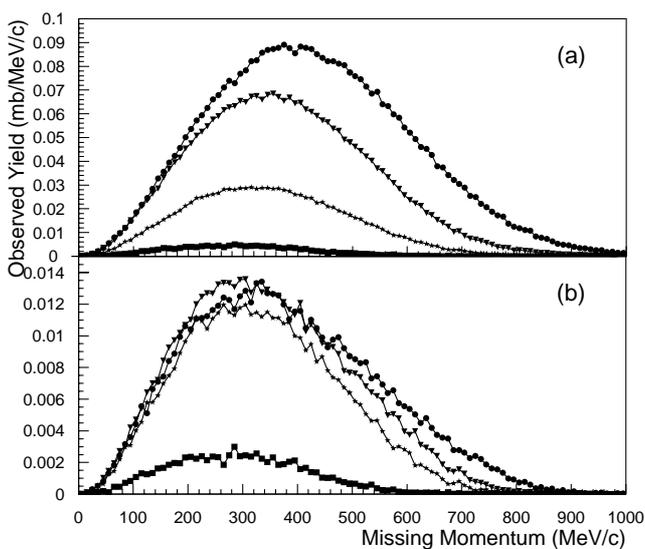
The number of incident pions was determined by the beam defining counters. To determine the number of pions which actually hit the target the counted pion rate was corrected for effects such as beam contamination with muons, pions lost through decay, pions lost through reactions in the scintillator and target, and pions missing the target. The largest correction came from the beam excluded by the target radial cut. The amount of beam excluded by this cut varied from 30% at the lowest pion energy (70 MeV) to 8% for the highest energy (239 MeV). Other beam flux corrections were small, typically 1-4%. The dominating error comes from the beam-missing-target correction. The pion flux upstream and downstream of the target was examined and the error was estimated to be half of the difference between the flux missing the target upstream and downstream (typically 5%-10%). The final normalization errors were in the range 6%-10%, except at the lowest pion energy where it was 20%.

C Monte Carlo Simulations

Monte Carlo simulations were performed to correct the data for the acceptance and inefficiencies of the detector and to assist in the interpretation of the data. In the simulations, the particles were tracked through a model of the detector using the CERN GEANT software package. The experimental resolutions and hardware thresholds, as determined from the data for each scintillation counter and MWPC, were applied to the simulated events. The simulated data were then analyzed with the same set of programs as was used for the measured data. The effects of geometrical acceptance, energy thresholds and reaction losses in the detector, as well as inefficiencies of the wire chambers and the reconstruction code, were thus reflected in the simulated distributions in the same way as in those of the experimental data. The reliability of this procedure, including the accuracy of the GEANT model of proton reactions at low energy, were tested earlier [14,19].

Four event generators were used to model the $(\pi^+, 3p)$ reaction. In each case a weight was included to represent the residual nucleus (spectator) momentum. This weighting factor was

$$\exp\left[-0.5 * (P_{res}/\sqrt{3} * P_{fermi})^2\right]$$

where P_{res} is the residual nucleus momentum and P_{fermi} reflects the width of the Fermi distribution. The value of P_{fermi} was adjusted to 110 MeV/c to reproduce the average missing momentum. This value is similar to those used by Tacik et al. [4] and Bauer et al. [5]. The residual nucleus can be in an excited state, and so the events were generated with an excitation energy distribution from 0 to 50 MeV. As in previous work [4] it was found that a simple flat distribution in the excitation energy was sufficient.

The simplest event generator created final states with three protons distributed uniformly over the phase space, but weighted as described just above. The second event generator was similar, but the events were weighted additionally by the Legendre polynomial $[1 - P_2(cos(\xi))]$ to

reflect contributions of total initial orbital angular momentum $L \geq 1$ as proposed by Šimičević and Mateos [20].

The other two event generators modelled simple two-step cascade processes: either an initial state interaction (ISI) followed by 2NA, or 2NA followed by a (hard) final state interaction (FSI). In the ISI model the incident pion was first scattered on a proton having a momentum randomly selected from a Fermi distribution. The scattering was generated according to the elastic πN cross section calculated with the phase shift code SCATPI [21]. In the second step the pion was absorbed on the quasi-deuteron according to the deuteron cross section [22]. The suppression of the forward pion quasi-elastic cross section due to binding effects was achieved with a weighting factor that fell linearly from unity to zero between 500 MeV/c and 250 MeV/c proton recoil momentum and stayed zero for protons with momentum below 250 MeV/c. In the FSI simulation, the pion was first absorbed on the quasi-deuteron and then one of the outgoing protons was scattered from a proton according to its elastic NN cross section, calculated with SAID [23]; a minimum momentum transfer of 150 MeV/c was required in this case. In both cascade models the energy needed to break up the nucleus (Q-value) was included in the kinematics of the absorption step.

D Fits and Efficiency Corrections

The fitting and acceptance correction method followed very closely the procedure used in our earlier work [14]. The 3p events which passed all the cuts described earlier were entered in a two-dimensional histogram of proton kinetic energy T_p versus proton polar angle θ_p. Since each proton was entered in the histogram there were three entries per event. Monte Carlo histograms for all event generators were created in three different ways:

LADSON30: All simulated events were run through the analysis chain with the same cuts and resolutions as for the real data. A proton threshold of 30 MeV was applied.

LADSOFF30: For these histograms the raw event generator data at the interaction vertex was used. These events were neither passed through the detector simulation nor through the analysis chain. All protons had to be above 30 MeV kinetic energy, but no other cuts were applied.

LADSOFF0: These distributions were the same as LADSOFF30 without the minimum kinetic energy requirement.

The LADSON30 distributions were fitted to the measured two-dimensional histogram (T_p vs. θ_p) with the normalizations of the event generators as free parameters. The efficiency corrected histograms were finally obtained with the formula

$$N(x) = N_{exp}(x) \frac{\sum_i p_i \times LADSOFF30_i(x)}{\sum_i p_i \times LADSON30_i(x)}$$
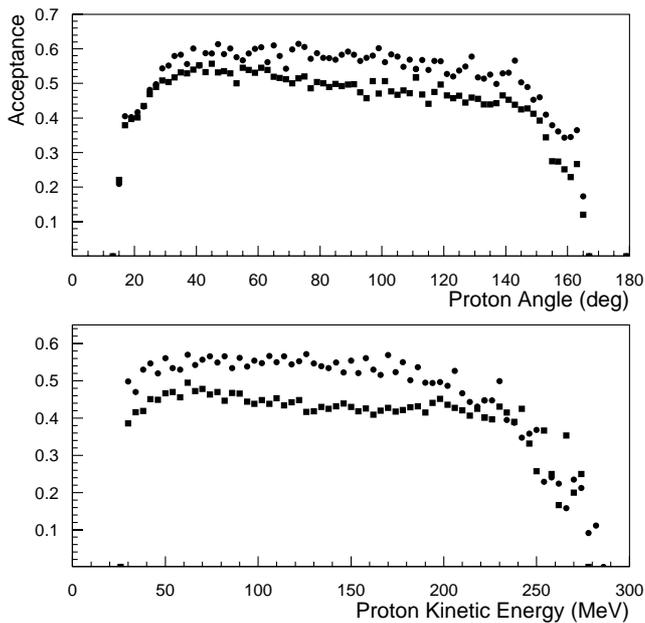
Fig. 9. The detector acceptance as determined by Monte Carlo simulations shown for the proton polar angle and the proton kinetic energy. Results using simulations with two models are presented: ISI (*circles*) and phase-space L≥0 (*squares*). A threshold of 30 MeV was applied

where i represents each of the event generators, p_i are the fitted normalization parameters and $N_{exp}(x)$ is the channel content of the experimental data.

In Fig. 9 typical examples of differential efficiencies as a function of the proton kinetic energy and polar angle are shown. In this plot all losses caused by the MWPCs, the reconstruction code, reaction losses in the scintillators, uncovered acceptance, etc are reflected. The two curves shown correspond to two models (out of the four) used in the simulation. The average difference in the detector acceptance calculated for these two extreme models was about 20%. The average efficiency with a 30 MeV threshold was of the order of 50%, and varied slightly with the incident pion energy. Even when an extrapolation to zero threshold was made, with the LADSOFF0 replacing the LADSOFF30 distributions in the above formula, the average efficiency remained about 30%.

IV Results

A Differential distributions

The projections of the two-dimensional histograms onto the θ_p and T_p axes are shown in Fig. 10 and 11. The plots show normalised cross sections corrected for detector acceptance and inefficiencies as described in Sect. B and D. Some non-smooth features of the data in the angular distributions reflect residual acceptance correction problems. A similar comment applies to the low energy region of the proton kinetic energy plots: sudden rises in the cross section at low energy (e.g. for Ar at 70 MeV) are most likely
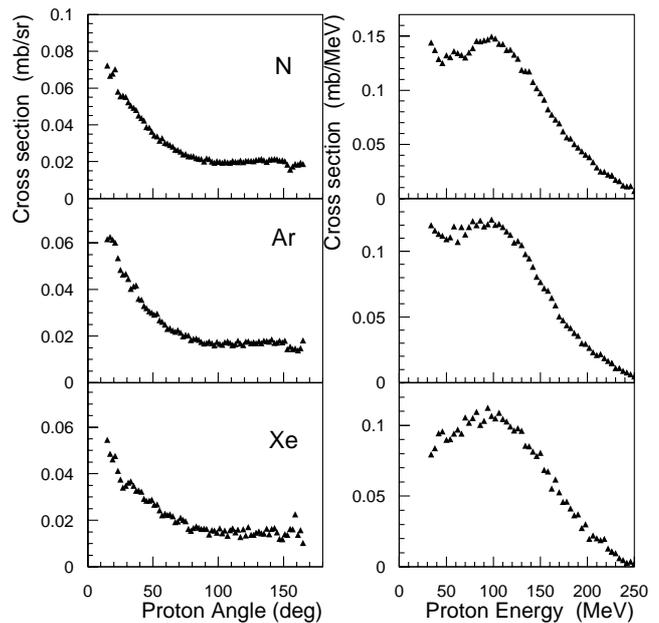

Fig. 10. Polar angle and kinetic energy distributions for the protons from the $(\pi^+, 3p)$ reaction at 239 MeV. The data have been corrected for the detector acceptance

unphysical. The data in this energy region (30-40 MeV) are very sensitive to the accuracy of the relative calibration of the ΔE and E counters, and to the accuracy of the calculation of the energy loss of the protons passing through the target walls and the target material. The accuracy of the simulation is insufficient to correct reliably for this effect.
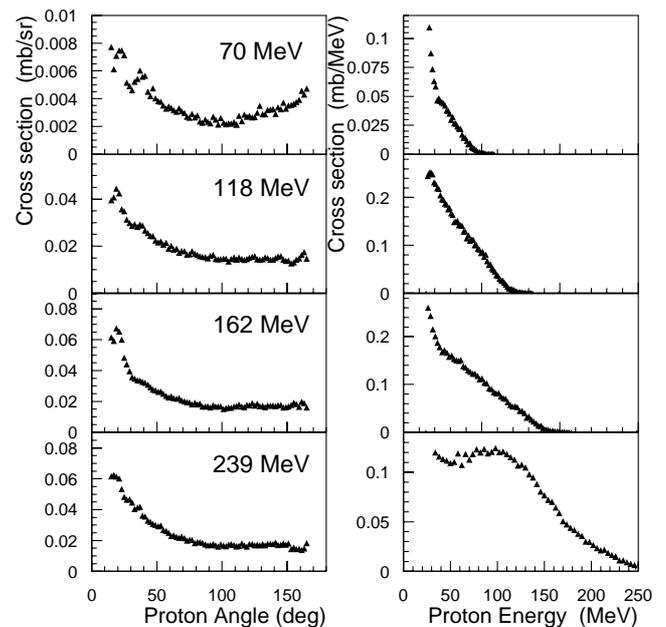

Fig. 11. Polar angle and kinetic energy distributions for the protons from the Ar$(\pi^+, 3p)$ reaction at four π^+ energies. The data have been corrected for the detector acceptance
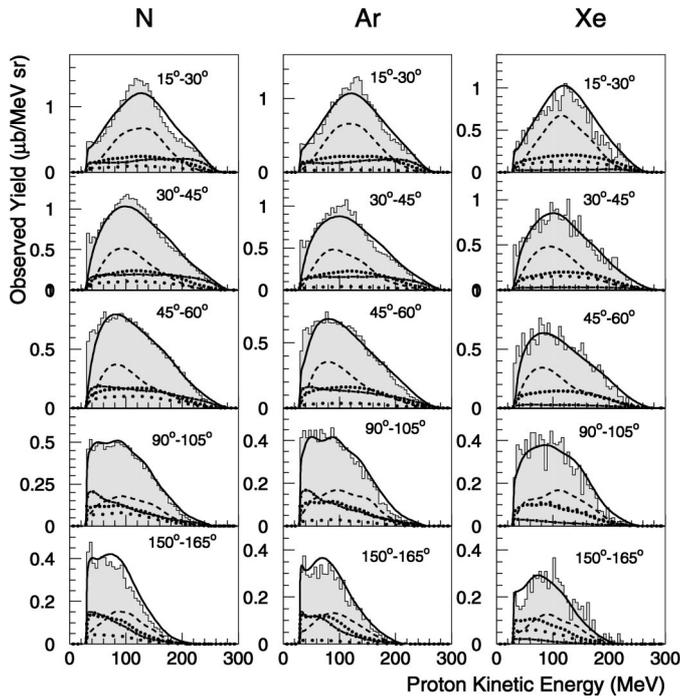
Fig. 12. The proton kinetic energy distributions for the $(\pi^+, 3p)$ reaction at 239 MeV, plotted in $15°$ slices for the N, Ar and Xe targets. The shaded area is the data and the solid line is the total Monte Carlo fit. Other lines show various components of the fits: ISI (*dashed*), FSI (*dashed-dotted*), phase-space $L \geq 1$ (*dotted*) and phase-space $L \geq 0$ (*wide dotted*)
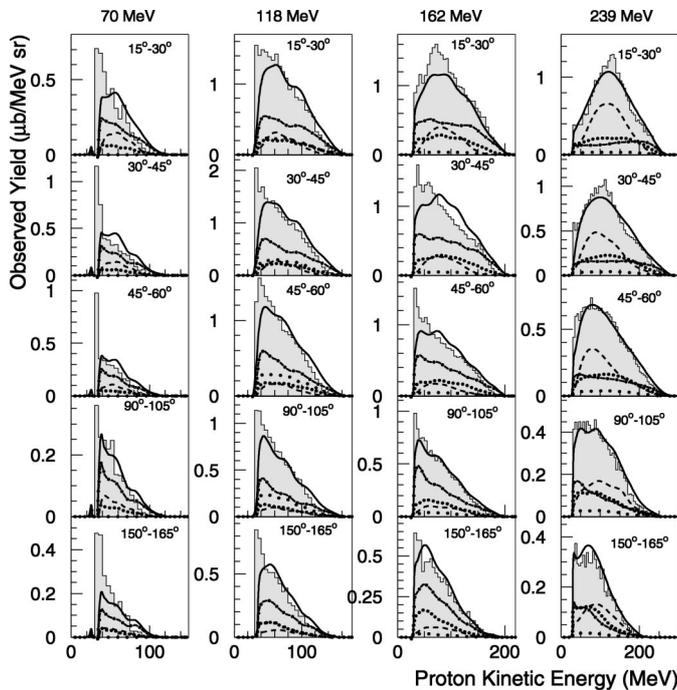

Fig. 13. The proton kinetic energy distributions for the Ar$(\pi^+, 3p)$ reaction at four π^+ energies plotted in $15°$ slices. The shaded area is the data and the solid line is the total Monte Carlo fit. Other lines show various components of the fits: ISI (*dashed*), FSI (*dashed-dotted*), phase-space $L \geq 1$ (*dotted*) and phase-space $L \geq 0$ (*wide dotted*)

Figures 12 and 13 show proton energy distributions for all targets and pion energies, compared to the results of the fits. In each of the two figures five angular bins are shown per energy and target. The quality of the fits is good for all three targets at the pion beam energy of 239 MeV. For the Ar data at the three other pion energies the fits are somewhat worse. This is especially true for the 70 MeV data, where the low proton kinetic energy data were affected by the problems discussed in the previous paragraph.

B ISI contribution

As can be seen in Figs. 12 and 13 the ISI model dominates the fits to the data in the forward angular slices. No model except ISI gives the peak in the kinetic energy distribution, which coincides with the free π^+-p scattering kinematics. Attempts to fit the data without the ISI model, that is with the FSI and PS models only, were unsuccessful. However, the data could be fitted with either the FSI or the PS contributions set to zero, without much loss in the fit quality. Therefore, no conclusions on the strength of FSI will be made in this work.

The fractional ISI strengths (corrected for acceptance) determined from these fits are shown in Table I and in Figs. 14 and 15. The errors quoted include the fitting error, the systematic error related to the data analysis method (*e.g.* selection of the data cuts) and an estimate of the model dependence. The fitting errors are those given by the fitting routine and are equal to about 0.04 (absolute error on the ISI fraction) except for the lowest energy where it is 0.1. In order to estimate the dependence of the results on the analysis method the procedure was repeated using modified cuts, e.g. the missing energy cut was varied between 30 MeV and 70 MeV. A cut on the missing momentum (of 500 MeV/c) was also introduced. Different assumptions about the initial momentum distributions were tested. All these variations resulted in final ISI fractions which were within 0.03 of the central value. Finally the dependence on the selection of the models was checked. This appeared to be the largest source of uncertainty. Switching various models on and off produced variations in the ISI fraction of ± 0.1. The results shown in

Table 1. The cross section for the $(\pi^+, 3p)$ reaction with a 50 MeV excitation energy cut. Also shown is the ISI fraction. The results are presented for a 30 MeV and a 0 MeV proton threshold

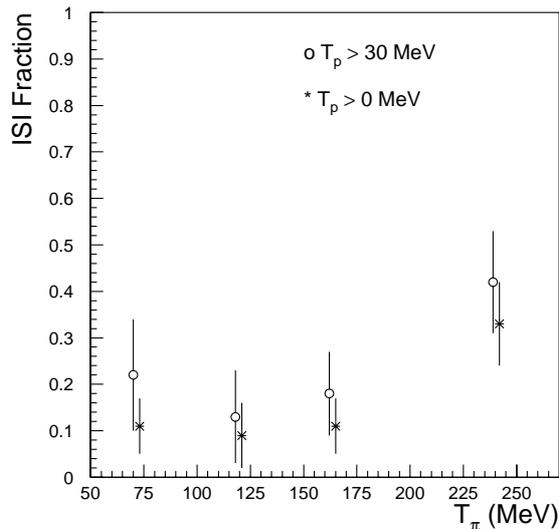| Target	T_π (MeV)	$T_p > 30MeV$ $\sigma_{(3p)}$ (mb)	ISI fraction	$T_p > 0MeV$ $\sigma_{(3p)}$ (mb)	ISI fraction
Ar	70	0.84±0.17	0.22±0.12	3.1±1.2	0.11±0.06
Ar	118	4.5±0.6	0.13±0.10	10.5±3.5	0.09±0.07
Ar	162	5.5±0.9	0.18±0.09	10.1±2.3	0.11±0.06
Ar	239	5.7±0.6	0.42±0.11	7.7±1.8	0.33±0.09
N	239	6.8±0.8	0.38±0.13	8.3±1.8	0.30±0.10
Xe	239	5.5±0.8	0.46±0.12	7.3±1.9	0.39±0.10

Fig. 14. The ISI fraction of the total $3p$ cross section for the $Ar(\pi^+,3p)$ reaction, with the excitation energy below 50 MeV, as a function of pion energy. The crosses show an estimate of the ISI fraction if all cross sections are extrapolated to 0 MeV threshold

Table I include all these errors added in quadrature. The data for the 0 MeV threshold have higher relative errors due to the extrapolation uncertainty.

The fraction of the $3p$ cross section assigned to the ISI process increases with the pion energy, becoming substantial (30%-40%) at 239 MeV. However, the ISI fraction at 239 MeV stays roughly constant with the target mass. It is interesting that the results presented here are similar to those for ^{4}He data [14], implying that the ISI mechanism is of similar importance from ^{4}He to Xe. For ^{3}He, however, there are differences, particularly at the lower
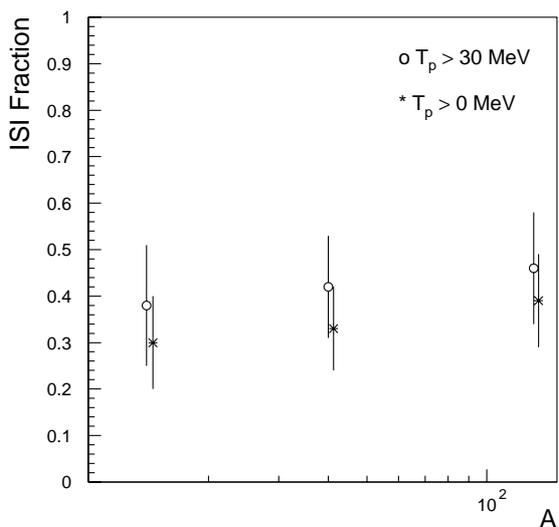

Fig. 15. The ISI fraction of the total $3p$ cross section for the $(\pi^+,3p)$ reaction at 239 MeV as a function of the target mass, with the excitation energy below 50 MeV. The crosses show an estimate of the ISI fraction if all cross sections are extrapolated to 0 MeV threshold

energies [14], where the ISI signal appears to be more significant than in all heavier nuclei.

As described in the introduction to this paper, prior to the LADS measurement there was little direct evidence for the existence of ISI in pion absorption. Brückner et al. [12] did not report a quantitative value for the ISI cross section, but an estimate, based on the published histograms, is consistent with our measurement. Two other experiments [2,4] which set upper limits on the contributions from ISI processes are also consistent with our data.

C Integrated cross sections

Table 1 and Figs. 16 and 17 show the $3p$ cross sections for events with the missing energy cut at 50 MeV. The cross sections are presented for two cases, with the proton threshold of 30 MeV and with no energy threshold. In the first case the kinetic energy distributions are not extrapolated and the acceptance corrections are smaller (1.6-2.6). In the second case, where the cross sections are extrapolated down to 0 MeV threshold, the acceptance correction is between 2.7 and 4.2 and includes significantly more model dependence. The errors shown include the statistical error, normalization error, and the model dependence error added in quadrature. The statistical errors are very small in all cases ($< 1.5\%$). The model dependence error was estimated by switching off various models used in calculating the acceptance correction. For example, for Ar at 239 MeV, using only the ISI or only the FSI model yields an acceptance correction which is 5% higher or 6.5% lower, respectively. This uncertainty becomes larger when dealing with the cross sections extrapolated to 0 MeV threshold. This is due to the fact that our models, used in the analysis, predict quite different low energy proton distributions. For example the FSI model predicts a large cross section for low energy protons, with the acceptance correction being 28% larger than that used in the final results. The simple phase space model has relatively little cross section for low energy protons and the acceptance correction is 15% lower than that used in the final results.

The 0 MeV threshold cross sections presented in Table I can be compared to the total pion absorption cross sections [18,24]. The $3p$ cross sections (with the 50 MeV cut) never exceed 10% of the absorption cross sections. The ratio of the $3p$ to the total absorption cross section decreases from 8% for N to 1% for Xe at 239 MeV. For the Ar target it varies with pion energy between 2% to 4% except at the lowest energy where it is only 1%.

Most of the previously published data did not have a 50 MeV missing energy cut similar to the one used in the present work. Tacik et al. [4] measured 22.9 mb for the $3p$ cross section on C at 228 MeV, which, because of our energy cut, is much larger than our N cross section of 8.3 mb. Our cross section without the 50 MeV missing energy cut, corrected with a rough estimate for the acceptance over the full missing energy, is about 30 mb. The BGO-Ball [6] cross sections are also, as expected, larger than ours. Their value of 25 mb for C is consistent with our estimate for N of 30 mb without the energy cut. However, our Ar
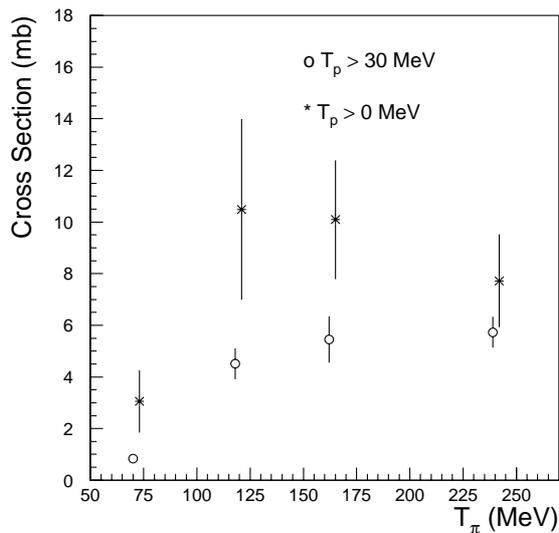
Fig. 16. The total cross section for the $Ar(\pi^+,3p)$ reaction with the missing energy cut at 50 MeV, as a function of pion energy. The squares represent the cross section measured with the 30 MeV proton threshold and the crosses the cross section extrapolated to 0 MeV threshold, shifted slightly to the right for clarity

and Xe cross sections without the 50 MeV cut are only about half of the BGO-Ball Ni and Sn data. This may not be surprising, as the BGO-Ball data do not exclude events containing one detected neutral particle in addition to the three protons.
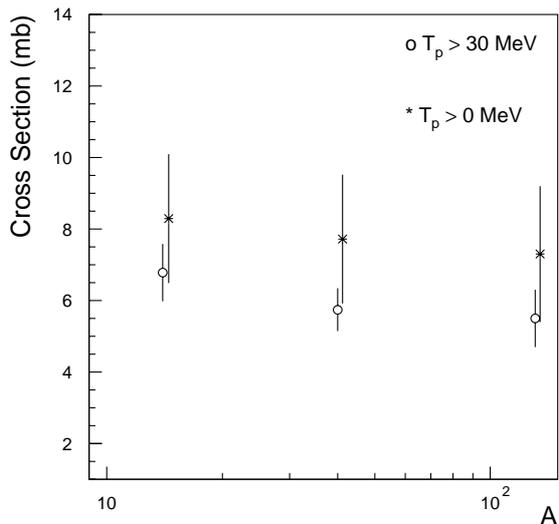

Fig. 17. The mass dependence of the total cross section for the $(\pi^+,3p)$ reaction at 239 MeV with the missing energy cut of 50 MeV. The squares represent the cross section measured with the 30 MeV proton threshold and the crosses the cross section extrapolated to 0 MeV threshold, shifted slightly to the right for clarity

V Summary

In the present paper we have presented the $3p$ absorption cross section with a 50 MeV cut on the excitation energy. This cross section never exceeds 10% of the total absorption cross section.

We have shown results of a direct measurement of the ISI process in pion absorption on heavy nuclei. The ISI signal was identified by its kinematic signatures, making full use of the 4π LADS detector. The cross section fraction assigned to the ISI process in the $3p$ channel varies considerably with the pion energy and stays roughly constant with the target mass. It is substantial (30%-40%) at only one pion energy, 239 MeV.

An attempt was made to search for an FSI signal in the $3p$ data. No kinematic variable was found to have sensitivity sufficient to distinguish the FSI process from the simple phase space distribution. Both the FSI Monte Carlo and the phase space Monte Carlo (together with ISI) gave good quality fits to the measured data, and therefore no statement about the strength of the FSI signal can be made. Since the magnitude of the ISI process never exceeds 50%, the reaction mechanism for most of the $3p$ cross section remains unexplained in terms of multi-step processes.

References

1. A. Altman, D. Ashery, E. Piasetzky, J. Lichtenstadt, A.I. Yavin, W. Bertl, L. Felawka, H.K. Walter, R.J. Powers, R.G. Winter and J.v.d.Pluym. Phys. Rev. **C34**, 1757 (1986)
2. W.J. Burger, E. Beise, S. Gilad, R.P. Redwine, P.G. Roos, N.S. Chant, H. Breuer, G. Ciangaru, J.D. Silk, G.S. Blanpied, B.M. Preedom, B.G. Ritchie, M. Blecher, K. Gotow, D.M. Lee and H. Ziock, Phys. Rev. **C41**, 2215 (1990)
3. D.J. Mack, P.G. Roos, H. Breuer, N.S. Chant, S.D. Hyman, F. Khazaie, B.G. Ritchie, J.D. Silk, G.S. Kyle, P.A. Amaudruz, Th.S. Bauer, C.H.Q. Ingram, D. Renker, R.A. Schumacher, U. Sennhauser and W.J. Burger, Phys. Rev. **C45**, 1767 (1992)
4. R. Tacik, E.T. Boschitz, W. Gyles, W. List, C.R. Otterman, W. Wessler, U. Wiedner and R.R. Johnson, Phys. Rev. **C40**, 256 (1989)
5. Th.S. Bauer, R. Hamers, P. Boberg, H. Breuer, R. van Dantzig, F. Geerling, S. Hyman, J. Konijn, C.T.A.M. de Laat, Y. Lefevre, A. Tall, J.L. Visschers and R. Ykema, Phys. Rev. **C46**, R20 (1992)
6. M.K. Jones, R.D. Ransome, V.R. Cupps, R.W. Fergerson, C.L. Morris, J.A. McGill, J.D. Zumbro, J.R. Comfort, B.G. Ritchie, J.R. Tinsley, P.G. Gugelot and C.F. Moore, Phys. Rev. **C48**, 2800 (1993)
7. C.H.Q. Ingram, Nucl. Phys. **A553**, 573c (1993)

8. H.J. Weyer, Phys. Rep. **195**, 295 (1990)
9. J.W. Negele and K. Yazaki, Phys. Rev. Lett. **47**, 71 (1981)
10. S. Fantoni, B.L. Friman and V.R. Pandharipande, Phys. Lett. **104B**, 89 (1981)
11. S.D. Hyman, D.J. Mack, P.G. Roos, H. Breuer, N.S. Chant, G.S. Kyle, P.A. Amaudruz, Th.S. Bauer, C.H.Q. Ingram, D. Renker, R.A. Schumacher, U. Sennhauser and W.J. Burger, Phys. Rev. **C47**, 1184 (1993)
12. W. Brückner, H. Dobbeling, P.C. Gugelot, F. Guttner, H. Kneis,S. Majewski, M. Nomachi, S. Paul, B. Povh, R.D. Ransome, T.A. Shibata,M. Treichel, Th. Walcher, P.A. Amaudruz, Th.S. Bauer, J. Domingo, R. Frey, C.H.Q. Ingram, H. Jantzen, G.S. Kyle, D. Renker and R.A. Schumacher, Nucl. Phys. **A469**, 617 (1987)
13. G. Backenstoss, D. Bosnar, H. Breuer, H. Döbbeling, T. Dooling, M. Furić, P.A.M. Gram, N.K. Gregory, A. Hoffart, C.H.Q. Ingram, A. Klein, K. Koch, J. Köhler, B. Kotliński, M. Kroedel, G. Kyle, A. Lehmann, A.O. Mateos, K. Michaelian, T. Petković, R.P. Redwine, D. Rowntree, U. Sennhauser, N. Šimičević, R. Trezeciak, H. Ullrich, M. Wang, M.H. Wang, H.J. Weyer, M. Wildi and K.E. Wilson, Phys. Lett. **B379**, 60 (1996)
14. A. Lehmann, D. Androić, G. Backenstoss, D. Bosnar, H. Breuer, H. Döbbeling, T. Dooling, M. Furić, P.A.M. Gram, N.K. Gregory, A. Hoffart, C.H.Q. Ingram, A. Klein, K. Koch, J. Köhler, B. Kotliński, M. Kroedel, G. Kyle, A.O. Mateos, K. Michaelian, T. Petković, M. Planinić, R.P. Redwine, D. Rowntree, U. Sennhauser, N. Šimičević, R. Trezeciak, H. Ullrich, M. Wang, M.H. Wang, H.J. Weyer, M. Wildi and K.E. Wilson, Phys. Rev. **C55**, 2931 (1997)
15. D. Androić, G. Backenstoss, D. Bosnar, H. Breuer, H. Döbbeling, T. Dooling, M. Furić, P.A.M. Gram, N.K. Gregory, A. Hoffart, C.H.Q. Ingram, A. Klein, K. Koch, J. Köhler, B. Kotliński, M. Kroedel, G. Kyle, A. Lehmann, A.O. Mateos, K. Michaelian, T. Petković, R.P. Redwine, D. Rowntree, U. Sennhauser, N. Šimičević, R. Trezeciak, H. Ullrich, M. Wang, M.H. Wang, H.J. Weyer, M. Wildi, and K.E. Wilson, Phys. Rev. **C53**, R2591 (1996)
16. T. Alteholz, D. Androić, G. Backenstoss, D. Bosnar, H. Breuer, A. Brković, H. Döbbeling, T. Dooling, W. Fong, M. Furić, P.A.M. Gram, N.K. Gregory, J.P. Haas, A. Hoffart, C.H.Q. Ingram, A. Klein, K. Koch, J. Köhler, B. Kotliński, M. Kroedel, G. Kyle, A. Lehmann, Z.N. Lin, G. Mahl, A.O. Mateos, K. Michaelian, S. Mukhopadhyay, T. Petković, M. Planinić, R.P. Redwine, D. Rowntree, R. Schumacher, U. Sennhauser, N. Šimičević, F.D. Smit, G. van der Steenhoven, D.R. Tieger, R. Trezeciak, H. Ullrich, M. Wang, M.H. Wang, H.J. Weyer, M. Wildi and K.E. Wilson, Nucl. Instrum. Methods **A373**, 374 (1996)
17. T. Alteholz, D. Androić, G. Backenstoss, D. Bosnar, H. Breuer, A. Brković, H. Döbbeling, T. Dooling, W. Fong, M. Furić, P.A.M. Gram, N.K. Gregory, J.P. Haas, A. Hoffart, C.H.Q. Ingram, A. Klein, K. Koch, J. Köhler, B. Kotliński, M. Kroedel, G. Kyle, A. Lehmann, Z.N. Lin, G. Mahl, A.O. Mateos, K. Michaelian, S. Mukhopadhyay, T. Petković, R.P. Redwine, D. Rowntree, R. Schumacher, U. Sennhauser, N. Šimičević, F.D. Smit, G. van der Steenhoven, D.R. Tieger, R. Trezeciak, H. Ullrich, M. Wang, M.H. Wang, H.J. Weyer, M. Wildi, and K.E. Wilson, Phys. Rev. Lett. **73**, 1336 (1994)
18. D.C. Rowntree, Ph.D. thesis, MIT Cambridge, (1995)
19. A. Mateos, Ph.D. thesis, MIT Cambridge, (1995); and to be published
20. N. Šimičević and A. Mateos, Phys. Rev. **C51**, 797 (1995)
21. SCATPI, J.B. Walter and G.A. Rebka, Los Alamos National Laboratory Report **LA-7731-MS**, (1979)
22. B.G. Ritchie, Phys. Rev. **C44**, 533 (1991)
23. R.A. Arndt, L.D. Roper, R.A. Bryan, R.B. Clark, B.J. VerWest, and P. Signell, Phys. Rev. **D28**, 97 (1983); R.A. Arndt, L.D. Roper, R.L. Workman and M.W. McNaughton, Phys. Rev. **D45**, 3995 (1992); SAID, R.A. Arndt et al., Virginia Polytechnic Institute and State University, (1988)
24. D. Ashery, I. Navon, G. Azuelos, H.K. Walter, H.J. Pfeiffer and F.W. Schlepütz, Phys. Rev. **C23**, 2173 (1981)